Learning from Correlations Based on Local Structure: Rare-earth Nickelates Revisited

Nicholas Wagner, Danilo Puggioni, and James M. Rondinelli*

Department of Materials Science and Engineering, Northwestern University, Illinois 60208-3108, USA

E-mail: jrondinelli@northwestern.edu

Abstract

Statistical analysis of local atomic distortions in crystalline materials is a powerful tool for understanding coupled electronic and structural phase transitions in transition metal compounds. The analyses of such complex materials, however, often require significant domain knowledge to recognize limitations in the available data, whether it be experimentally reported crystal structures, property measurements, or computed quantities, and to understand when additional experiments or simulations may be necessary. Here we show how additional descriptive statistics and computational experiments can help researchers explicitly recognize these limitations and fill in missing gaps by constructing amplitude (a) and normalized-amplitude (n) distortion-mode–property correlation-coefficient-heat maps, aCCHMs and nCCHMs, respectively. We demonstrate this utility within the rare-earth nickelate perovskites $R\mathrm{NiO_3}$ (R = rare earth $\neq$ La), which exhibit antiferromagnetic and metal-insulator transitions with crystallographic symmetry breaking, and analyze the CCHMs obtained from experimental and first-principles derived symmetry modes. In contrast with the crystallographic trends gleaned from the reported experimental structures, the equilibrium structures obtained from density functional theory indicate that the Jahn-Teller distortion mode

plays a negligible role in affecting the Néel temperature. We explain this discrepancy and discuss how different researchers might draw disparate conclusions from the same evidence, in particular from *a*CCHMs and *n*CCHMs. Last, we propose a general method for utilizing CCHMs for screening large databases of structures.

Introduction

As structure-property information on materials is collected into databases[1] to enable machine learning studies,[2,3] a sufficient level of accuracy and precision of the data is paramount for making meaningful predictions from data-derived models. Crystal structures are a common type of data in materials science that are recorded in databases such as the Inorganic Crystal Structure Database (ICSD)[4] and Crystallography Open Database (COD).[5,6] These structures, which are often solved using scattering methods at finite temperature, are widely used to benchmark *ab initio* methods such as density functional theory (DFT), which is formally a 0 K ground-state theory.[7,8] Because the structure of materials dictate materials properties, they are frequently examined to develop processing-property relationships for materials engineering. These relationships can vary in length scale, from atomic picoscale structure within the unit cell to microstructure morphology, and in scope: studying the optical behavior of a single chemical compound,[9] exploring the origins of symmetry-breaking in a whole class of materials,[10] and examining trends in superconducting critical temperatures across enormous databases of first-principles calculations.[11]

There are various approaches for translating crystal structures into numerical features appropriate for use in statistical analysis and machine learning. Within the last year alone, several useful approaches were developed, including many-body tensors,[12] Voronoi tessellations,[13] and crystal graphs.[14] One approach, which finds widespread application in the ABX_3 perovskite literature, is to use representation theory and symmetry-based mode

distortion modes to describe changes in crystal structure with respect to a high-symmetry structure.[15,16] These distortion modes transform as irreducible representations (irrep) of the crystallographic space groups and allow one to describe cooperative bond-length distortions and octahedral rotations in perovskites (as well as many other structure types) with coupled lattice degrees of freedom with an orthogonal basis set. In addition, materials chemists already recognize the utility of mode crystallography[17] and the importance of these microscopic atomic degrees-of-freedom to serve as proxies for structural and electronic transitions.[18–21] When a phase transition occurs at a finite temperature, T, the active distortion mode $\vec{\eta}$ would suffice to serve as the order parameter. The amplitudes of these distortion modes therefore can act as a highly interpretable set of features that can be used in statistical analysis of such compounds with interdependent degrees-of-freedom.[22]

Rare-earth nickelate perovskites $R\mathrm{NiO_3}$ (R = rare earth $\neq$ La) exhibit a rich phase diagram[23] and are well-suited for assessing and understanding the feasibility of learning from symmetry-mode–property correlations owing to the multiple lattice degrees-of-freedom they exhibit (Fig. 1). At high temperature, these compounds are paramagnetic metals and exhibit the orthorhombic *Pnma* space group commonly adopted by perovskite oxides with crystallographic tolerance factors less than unity, indicating that the R cation is too small to fit in the cavities created by the corner-connected $\mathrm{NiO_6}$ octahedra. The orthorhombic tilt system is characterized by out-of-phase rotations of the $\mathrm{NiO_6}$ octahedra about two axes while the rotations between adjacent octahedra occur in-phase about the third axis. Upon cooling, these nickelates undergo a concomitant orthorhombic-to-monoclinic structural transition ($Pnma \rightarrow P2_1/c$) and a metal-insulator transition (MIT). We note that while the *Pnma* and $P2_1/c$ space group settings are the standard settings for space group numbers 62 and 14, respectively, different authors may report the structures with orthorhombic distortion in the *Pbnm* setting or the monoclinic structure in the $P2_1/n$ setting. For consistency, all structures in this contribution use the *Pnma* and $P2_1/c$ settings. At even lower temperature, a long range antiferromagnetic ordering emerges. Note that in

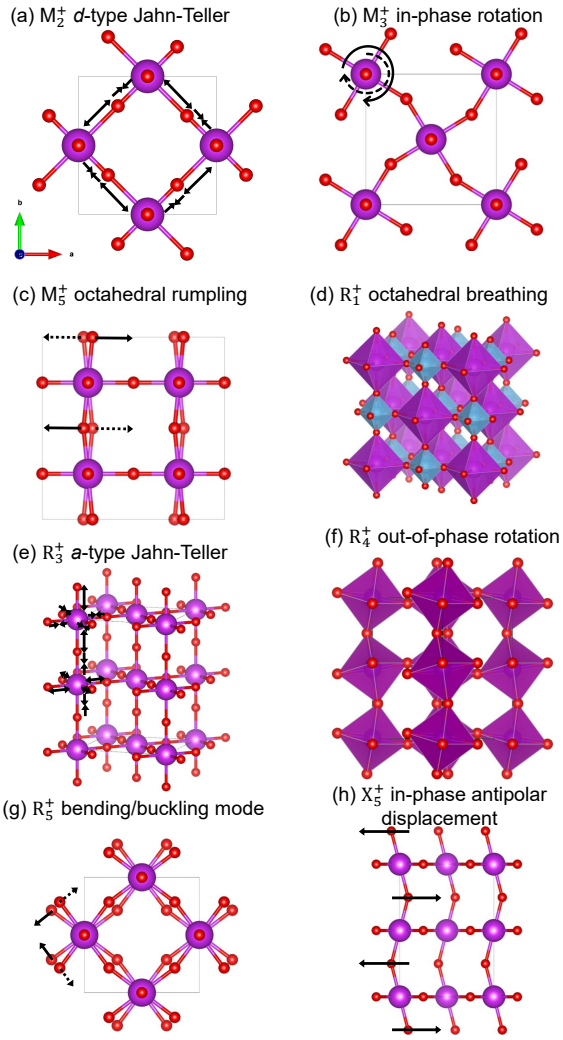

Figure 1: Illustration of distortion modes present in the monoclinic $P2_1/n$ RNiO$_3$ perovskites. The out-of-phase distortions are differentiated using arrows (lines and dashes) to indicate the direction of cooperative atomic displacements. (a) M_2^+ describes the planar *d*-type Jahn-Teller mode, where two bonds shrink and two elongate in every (001) plane. (b) M_3^+ describes an in-phase NiO$_6$ rotation mode about [001]. (c) M_5^+ describes an out-of-phase antipolar motion of the oxide anions. (d) R_1^+ describes an octahedral breathing mode, where alternating octahedra expand and contract. (e) R_3^+ describes the three-dimensional *a*-type Jahn-Teller mode, where four bonds contract and two elongate, and vice versa. (f) R_4^+ describes an out-of-phase NiO$_6$ rotation mode about [110]. (g) R_5^+ describes an out-of-phase NiO$_6$ bending mode. (h) X_5^+ describes in-phase antipolar oxide anion motion accompanied by R cation displacements, which are not shown for clarity.

general $T_N < T_{MI}$ across the nickelate family with the exceptions that $NdNiO_3$ and $PrNiO_3$ exhibit an MIT temperature (T_{MI}) coincident with the magnetic ordering temperature (T_N).

Starting from a fully localized electron picture in the RNiO$_3$ family, the nominal Ni oxidation state should be Ni^{3+} with the cations adopting a d^7 low-spin configuration, $t_{2g}^6 e_g^1$. Thus, it is expected that the metal-insulator transitions in these orbitally degenerate compounds arise from an orbital ordering within the Ni 3d manifold induced by a cooperative Jahn-Teller distortion.[24] However, because RNiO$_3$ are located within the localized-to-itinerant electron crossover regime, the MIT proceeds via an alternative 'charge-disproportionation' mechanism. The Ni^{3+} valence instability results in an ordered three-dimensional arrangement of an approximately Ni^{2+} (e_g^2 configuration) and Ni^{4+} (e_g^0) cations,[25] with strong oxygen-hole character.

From the structural point of view, the essential ingredient of the charge-ordering model is supported by the crystallography. The active *primary* distortion at the structural $Pnma \rightarrow P2_1/c$ transition is a NiO_6 octahedral breathing mode that transforms as the irrep R_1^+ (Fig. 1d). Such a dilation and contraction of the local NiO_6 unit is expected if there is intersite charge transfer. Interestingly, detailed inspection of the reported experimental $P2_1/c$ monoclinic structures shows that the octahedral breathing mode is accompanied by two *secondary* distortion modes, *i.e.*, an oxygen rumpling mode (irrep M_5^+, Fig. 1c) and an a-type Jahn-Teller distortion mode (irrep R_3^+, Fig. 1e). The previous observation of coexisting R_1^+ and R_3^+ modes in the experimental structures seems to suggest that charge ordering and Jahn-Teller distortions are not alternative (independent) routes[25] to remove the Ni^{3+} orbital degeneracy in RNiO$_3$, but rather cooperate (or perhaps compete) to remove it. Despite this indication of a cooperate-Jahn-Teller distortion in the experimental RNiO$_3$ structures, orbital ordering has never been observed experimentally.[26,27]

In 2013, Balachandran and Rondinelli showcased the use of the aforementioned distortion modes as structural descriptors for the critical temperatures in the RNiO$_3$ (R = rare earth $\neq$ La) family.[28] The authors concluded from a statistical analysis of the distortion

mode–property correlations that (*i*) counter-intuitively, the breathing mode R_1^+ has a moderate effect on T_{MI} and (*ii*) it could be possible to decouple the metal-insulator transition from the magnetic ordering transition by enhancing the secondary Jahn-Teller distortion mode R_3^+. Here, we present first-principles calculations on the rare earth nickelates to show that, firstly, the breathing mode exhibits strong positive correlation with T_{MI}, and that this original statement is appropriate when describing the nickelate family as a complete class. Secondly, the decoupling hypothesis, which arises from a local interpretation of the distortion-mode–property relationships, is not justified; it is due to an overextended interpretation of correlation-coefficient-heat maps (CCHMs) based on mode amplitudes rather than normalized-mode amplitudes, which we show can capture multi-mode interactions.

In addition, we use our results to conduct a new statistical analysis, and we report three main findings: First, the distortion-mode–property correlations obtained from DFT calculated crystal structures are in qualitative disagreement with those obtained using experimental crystal structures. Second, in agreement with other studies,[29] our simulations show the Jahn-Teller mode has a negligible effect on the stability of competing magnetic phases, which is accurately manifested in normalized-mode–mode correlation-coefficient-heat (*n*CCHMs) maps. Last, structural anomalies in closely related chemical families can be identified using descriptors applicable to high-throughput screenings. Our study demonstrates the importance of domain knowledge when trying to statistically infer structure–property relationships[30] especially in complex ternary oxides with nontrivial electronic and orbital interactions.

Methods

Density Functional Theory

First-principles calculations were performed with the Vienna *Ab initio* Simulation Package (VASP).[31] We employed the generalized gradient approximation revised for solids func-

tional (PBEsol)[32] in combination with a plus Hubbard U correction[33] of 2 eV on the Ni $3d$ states to account for electronic correlations in the nickelates.[34] We used a 550 eV planewave cutoff and projector-augmented wave (PAW) pseudopotentials with the following electron configurations: $4s^2 3d^8$ (Ni), $2s^2 2p^4$ (O), $6s^2 5p^6 5d^1$ (Lu), $6s^2 5p^6 5d^1$ (Er), $6s^2 5p^6 5d^1$ (Ho), $4s^2 5s^1 4p^6 4d^2 4f^0$ (Y), $6s^2 5p^6 5d^1$ (Dy), $6s^2 5p^6 5d^1$ (Tb), $6s^2 5p^6 5d^1$ (Gd), $6s^2 5p^6 5d^1$ (Eu), $5s^2 6s^2 5p^6 5d^1$ (Sm), $5s^2 6s^2 5p^6 5d^1$ (Nd), $5s^2 6s^2 5p^6 5d^1$ (Pr). Brillouin zone integrations were performed using a $3 \times 6 \times 2$ Γ-centered k-point mesh.

We did not treat explicitly the magnetism of the rare-earth (R) electrons as they order at very low temperature, and we included the f-electrons as core electrons in the PAW pseudopotentials. Unless specified otherwise, we use crystal structures where the cell angles are fixed to the experimental value of $NdNiO_3$ at 50 K[35] and the ions and lattice constants are relaxed until the Hellmann-Feynman forces are less than 1 meV $Å^{-1}$ and 0.1 GPa, respectively. Specifically, the atomic relaxations were performed within an 80-atom supercell with $P2_1/c$ symmetry to accommodate both collinear ferromagnetic (FM) and E′-type antiferromagnetic (AFM) spin order.[23,36] The E′-type AFM ordering is an '$\uparrow - \uparrow - \downarrow - \downarrow$' stacking sequence of ferromagnetically ordered Ni planes along the pseudocubic [111] direction, corresponding to a magnetic wavevector of $q = (1/4, 1/4, 1/4)$ in pseudocubic notation.

Representation Theory

The group theoretical analyses were performed with the AMPLIMODES software[37,38] using monoclinic structures from previous publications[35,39–41] and our DFT calculations. Nickelates with R = Lu, Yb, Tm, Er, Ho, and Y were measured at 295 K, $DyNiO_3$ at 200 K, $NdNiO_3$ at 50 K, and $PrNiO_3$ at 10 K. These temperatures were the same as those in the Balachandran and Rondinelli study (Ref. 28). Although one may expect some modest temperature dependence on the amplitudes upon cooling below the ordering temperatures, the general trends are not expected to change but only be made more pronounced. We

perform distortion-mode decompositions with respect to a high symmetry $Pm\bar{3}m$ phase and we neglect the strain and fully-symmetric modes. The distortion-mode amplitudes were normalized to the parent cell volume and we use these values throughout. There are eight symmetrically independent distortion modes in the $P2_1/c$ space group with the following irreducible representations (irrep): R_1^+, R_3^+, R_4^+, R_5^+, X_5^+, M_2^+, M_3^+, M_5^+. Of these modes, the orthorhombic *Pnma* also exhibits distortion modes transforming as R_4^+, R_5^+, X_5^+, M_2^+, M_3^+. Schematic illustrations of each irrep are given in Fig. 1.

Features, Learning Scheme, and Visualization

For our correlation analysis, we used the metal-insulator (T_{MI}) and Néel (T_N) ordering temperatures reported in the review by Catalan.[42] For all nickelates we use 8-coordinate ionic radii from Shannon[43] as published on the Atomistic Simulation Group's website[44] for comparing the size of the rare-earth cations in different nickelates. Although the R cations are expected to be 12-coordinate in cubic perovskites, the nickelates possess the $GdFeO_3$-type distortions, which reduce the R cation coordination. (The 12-coordinate radii are also unavailable for all rare-earth cations.) This radii choice does not qualitatively change our analysis.

The Python software packages `SciPy`,[45] `NumPy`,[46] `matplotlib`,[47] and `plotly`[48] were used for computing Pearson correlation coefficients and data visualization. Fig. 1 was made using the VESTA crystallographic software.[49]

The correlation-coefficient-heat maps (CCHMs) are constructed in two manners using the experimental and theoretical structural data. First, we use distortion-mode amplitudes (a) to construct aCCHMs. Unlike the approach of Ref. 28, whereby supervised regression learning is carried out on pre-processed data, *i.e.*, such that the mean is subtracted from each feature represented as a column (corresponding to a distortion mode or ordering temperature) and then each 'centered' column is normalized by its respective standard deviations, we chose not to perform this type of feature scaling on the mode amplitudes.

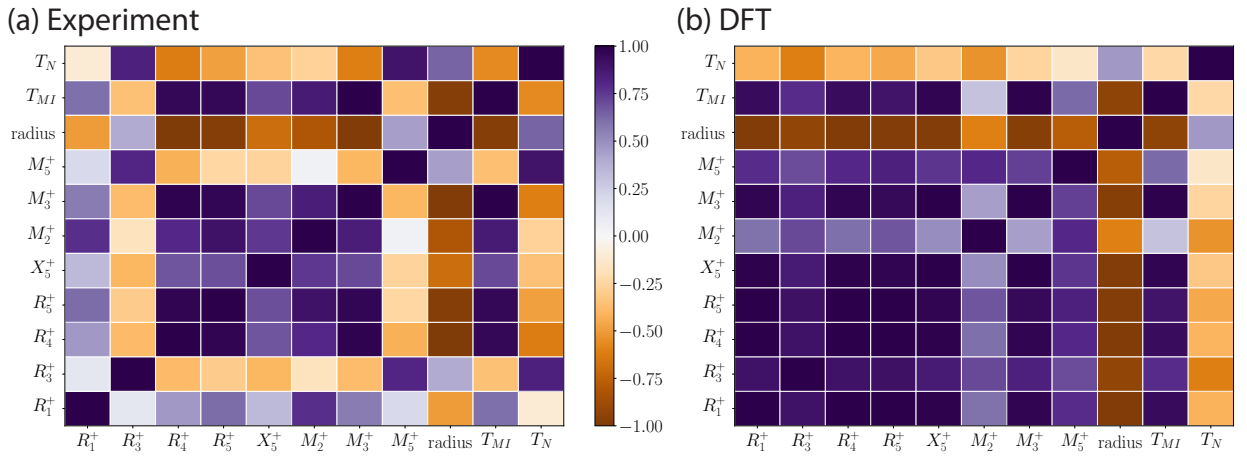

Figure 2: Amplitude correlation-coefficient-heat maps (*a*CCHMs) calculated from (a) experimentally published crystal structures and (b) from our DFT relaxed crystal structures. All ordering temperatures correspond to values from experiment.

Such scaling will not not affect the correlation coefficients, which is of our main interest since it captures how a change in one variable may affect the change in another; however, covariance is scale dependent. Second, we constructed mode-normalized correlation-coefficient-heat maps (*n*CCHMs) using the Euclidean norm of the total distortion vector[17] from the experimental and theoretical structural data. We emphasize that two types of correlations can be examined in these CCHMs: distortion-mode–property and distortion-mode–distortion-mode correlations, which we refer to in pair notation as for example, (η_i, T) and (η_i, η_j), respectively. Which type of CCHM is appropriate for understanding a given variable pair relationship is explored in detail below.

Results

Correlation-Coefficient Heat Maps

In Fig. 2a we generate the distortion-mode amplitude correlation-coefficient-heat map using the experimental crystal structures, which resembles the CCHM of Balachandran and Rondinelli (corresponding to Fig. 6 from Ref. 28). For completeness, we include $YbNiO_3$

Table 1: Crystallographic data for RNiO$_3$ compounds from DFT-PBEsol+U = 2 eV.[a]

R	Lu	Er	Ho	Y	Dy	Tb	Gd	Eu	Sm	Nd	Pr
a (Å)	5.19632	5.23195	5.24369	5.26943	5.25568	5.26800	5.28112	5.29538	5.31162	5.34338	5.36146
b (Å)	5.20659	5.24229	5.25405	5.27984	5.26607	5.27841	5.29156	5.30584	5.32211	5.35394	5.37206
c (Å)	8.99555	9.05722	9.07754	9.12210	9.09831	9.11963	9.14234	9.16702	9.19514	9.25012	9.28142
R 4e (x y z)											
x	0.26856	0.26603	0.26524	0.26383	0.26443	0.26361	0.26286	0.26196	0.26089	0.25859	0.25762
y	0.42914	0.43324	0.43500	0.43801	0.43686	0.43898	0.44153	0.44455	0.44854	0.45944	0.46655
z	0.24989	0.24989	0.24989	0.24989	0.24989	0.24989	0.24995	0.24996	0.24996	0.24999	0.24995
O1 4e (x y z)											
x	0.14380	0.15269	0.15555	0.16047	0.15867	0.16200	0.16561	0.16962	0.17395	0.18376	0.18853
y	0.02930	0.02320	0.02148	0.01949	0.01953	0.01752	0.01532	0.01310	0.01112	0.00706	0.00594
z	0.25589	0.25553	0.25544	0.25537	0.25532	0.25521	0.25488	0.25473	0.25461	0.25433	0.25405
O2 4e (x y z)											
x	0.36684	0.35950	0.35692	0.35290	0.35402	0.35081	0.34736	0.34318	0.33832	0.32567	0.31757
y	0.20161	0.20397	0.20499	0.20661	0.20608	0.20737	0.20917	0.21115	0.21371	0.22102	0.22667
z	0.05725	0.05301	0.05172	0.04934	0.05023	0.04865	0.04709	0.04523	0.04329	0.03878	0.03622
O3 4e (x y z)											
x	0.74056	0.74227	0.74250	0.74340	0.74282	0.74301	0.74238	0.74221	0.74160	0.73896	0.73670
y	0.30660	0.30419	0.30316	0.30168	0.30203	0.30069	0.29886	0.29683	0.29420	0.28660	0.28138
z	0.94311	0.94721	0.94849	0.95085	0.94994	0.95147	0.95279	0.9546	0.0.95656	0.96107	0.96378

[a] All structures exhibit $P2_1/c$ symmetry with cell angles $\alpha = \gamma = 90^\circ$ and $\beta = 125.225^\circ$; the Ni 2a site resides at $(0\ 0\ 0)$ and the Ni 2d site is at $(\frac{1}{2}\ 0\ \frac{1}{2})$.

and TmNiO$_3$ in Fig. 2a, in addition to the original (R=Lu, Er, Ho, Y, Dy, Nd, Pr)NiO$_3$ as done in Ref. 28. We note that the R=Yb and Tm monoclinic $P2_1/c$ structures[50] and ordering temperatures[51] were unavailable in 2013. Linear correlation-coefficient-heat map (CCHMs) plot the Pearson correlation coefficients, defined as the covariance of two variables divided by the product of their standard deviations, among the crystal-distortion modes and macroscopic transition temperatures, T_{MI} and T_N. We also show the correlation with the R ionic radii, denoted as "radius" in the CCHMs, in Fig. 2. Purple shades indicate positive linear correlation between the two features, whereas browner shades indicate negative linear correlation. Intermediate shades indicate no linear correlation exists between the two variables. In Fig. 2b, the same correlations are shown but using 11 DFT relaxed crystal structures corresponding to R = Lu, Er, Ho, Y, Dy, Tb, Gd, Eu, Sm, Nd, and Pr. The detailed structural information is provided in Table 1. For all nickelates, our calculations reproduce the insulating $P2_1/c$ AFM-E$'$ magnetic structure in agreement with Ref. 29.

We first compare the similarities between the experimental and theoretical correlation-coefficient heat maps, focusing on distortion-mode–property dependencies. Each structure

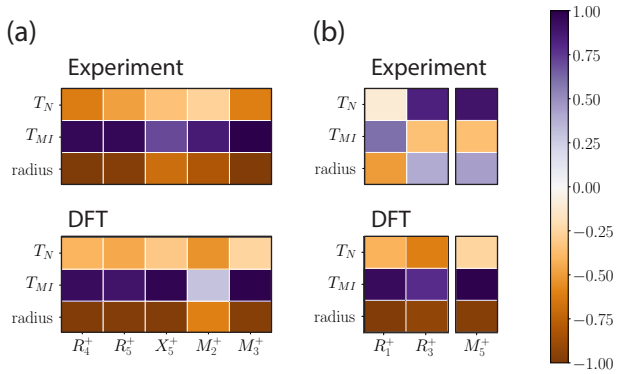

Figure 3: Slices of the *a*CCHM emphasizing (a) similarities and (b) differences from the experimentally published crystal structures and from our DFT relaxed crystal structures.

set shows that the distortion modes present before the $Pnma \rightarrow P2_1/c$ structural transition, *i.e.*, the *d*-type Jahn-Teller M_2^+ (Fig. 1a), in-phase rotations M_3^+ (Fig. 1b), out-of-phase rotations R_4^+ (Fig. 1f), bending/buckling R_5^+ (Fig. 1g), and the in-phase antipolar X_5^+ (Fig. 1h) modes, are all positively correlated with one another and T_{MI} (Fig. 3). Likewise, these modes are all negatively correlated with the rare earth ionic radius and T_N. Although the correlation coefficients for the antipolar X_5^+ and *d*-type Jahn-Teller M_2^+ modes are smaller in experiment than in DFT, the trend is qualitatively the same.

Now we examine the distortion-mode–property discrepancies between Fig. 2a and Fig. 2b. Special attention is paid to the breathing R_1^+ (Fig. 1d), *a*-type Jahn-Teller R_3^+ (Fig. 1e), and rumpling M_5^+ (Fig. 1c) modes as they arise at the $Pnma \rightarrow P2_1/c$, MIT transition (Fig. 3b). Repeating an observation from prior work about Fig. 2a, the NiO_6 octahedral breathing mode (R_1^+) exhibits nearly zero correlation with T_N and weak positive correlation with T_{MI} relative to the correlation of other distortion modes with T_N and T_{MI}. This observation, however, is at odds with the DFT correlations shown in Fig. 2b and Fig. 3b, which both indicate the breathing mode exhibits strong positive correlation with T_{MI}, $(R_1^+, T_{MI}) \sim 1$, and that it also has strong negative correlation with T_N, $(R_1^+, T_N) \sim -1$. These dependencies are clearly discerned in Fig. 3b. Furthermore, the correlation behavior for the primary experimental and DFT (R_1^+, radius) pairs are qualitatively the same, *i.e.*, the breathing mode is anti-correlated with the ionic radius, which is expected

given the nature of the nickelate phase diagram.

Next we consider how the the secondary distortion modes, the *a*-type Jahn-Teller R_3^+ mode and the octahedral rumpling M_5^+ mode, correlate with the ordering temperatures. The experimental structures show the correlation $(R_3^+, T_N) > 0$ whereas the DFT structures indicate strong negative correlation. In addition, it is the opposite sign of the correlation coefficients for the distortion-mode–property pairs (R_3^+, T_N) and (R_3^+, T_{MI}) in experimental data that suggests decoupling of the critical ordering temperatures, T_N from the T_{MI}, could be accomplished by boosting the relative amplitude of the R_3^+ mode independent of the other modes. We will show that our theoretical first principles calculations do not support this conjecture based on the *a*CCHMs. The ordering-temperature dependencies with M_5^+ are similar to those obtained for R_3^+ within the same structure data set.

We also find that the correlation behavior for the experimental and DFT secondary modes with the ionic radius are opposite. One explanatory factor for the discrepancy could be due to the definition of the Pearson correlation coefficient itself. As a simple measure of linear correlation, it can fail to describe well nonlinear trends in data or be skewed by outliers. This behavior, however, is not observed in our data as seen from the two-variable scatter plots appearing in Figures S1 and S2 of the Supporting Information (SI). We also note that the experimental *a*CCHM is based upon only 9 published $P2_1/c$ monoclinic structures (*R*=Lu, Yb, Tm, Er, Y, Ho, Dy, Nd, and Pr),[35,39–41,50] while the theoretical *a*CCHM is based upon 11 compounds (*R*=Lu, Er, Ho, Y, Dy, Tb, Gd, Eu, Sm, Nd, and Pr). A single reported structure could confound proper establishment of correlations if it varied in some manner with such a small sample number. We assessed this possibility by removing $NdNiO_3$ from the experimental data. We find that after removal the R_3^+ distortion mode and T_N are no longer correlated. Thus, $NdNiO_3$ plays an important role in the statistical analysis, as likely would $PrNiO_3$ because for these nickelates $T_{MI} = T_N$. To this end, we emphasize that when dealing with small structural data sets, "more data is better;" we state this in the sense that more structural data can increase the scope of conclusions that

can be drawn from symmetry-mode–property correlation maps of complex materials.

So far in our discussion we have mainly focused on structure-based property correlation pairs. Interestingly, upon examining the *distortion-mode–mode pairs*, we find the experimental- and DFT-based *a*CCHMs indicate the R_1^+ and R_3^+ modes are positively correlated with each other, despite evidence indicating that these distortion modes should be alternative local structure routes for removing the electronic degeneracy.[25] In other words, they should exhibit finite anti-correlation based on available domain-science models. Nonetheless, the DFT *a*CCHMs do capture, more so than the experimental *a*CCHMs, the dominant effect of the ionic radius on the distortion modes. The *R* radius sets the amplitudes of all the distortion modes and for that reason both the R_1^+ and R_3^+ modes depend together (and in an anti-correlated manner) with the ionic radius as seen in the DFT data (Fig. 2b). Indeed, materials-chemistry models show that the octahedral rotation and tilt modes induced by the size of the *R* cations define the degree of covalency in the $R\mathrm{NiO_3}$ family;[29] for that reason, the radius should correlate with both the stability of the magnetic ordering and the insulating phase and the local distortion mode driving the respective order. The anticipated mode-mode dependence, however, is not well reproduced. For that reason, no apparent insight is available from the *a*CCHMs about which distortion mode in particular should be modified to control ordering temperatures since the individual effects of the modes are subtler than the changes due to ionic radius variance. After assessing the uncertainty in the data sets in the next section, we show how this "missing" knowledge can be obtained by computational investigations into causation and ultimately captured in suitably constructed mode-normalized CCHMs.

Statistical Analysis

Visualizing statistics about the data can reveal relevant information about the variance of the features. The mean values and standard deviations of the breathing (R_1^+), *a*-type Jahn-Teller (R_3^+), and octahedral rumpling (M_5^+) mode amplitudes are shown in Fig. 4. The

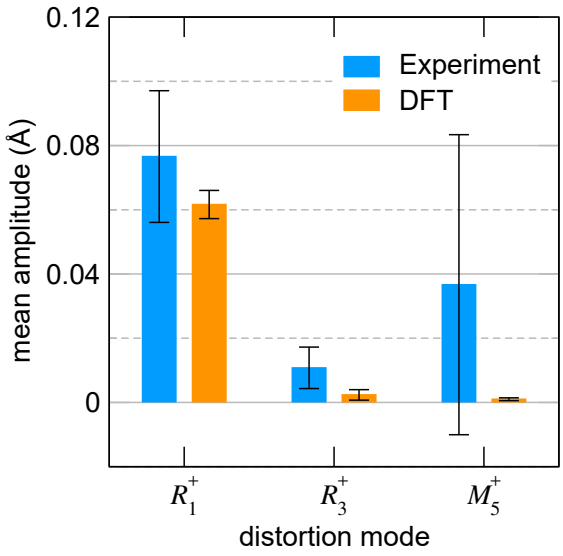

Figure 4: Comparison of the mean calculated and experimental monoclinic distortion-mode amplitudes. Bars represent plus/minus standard deviation from the mean.

experimental mean values are found to always be larger than that obtained from the DFT structures. In addition, the relative ranking of the mean amplitudes by distortion mode is not the same in the two data sets. The experimental structures exhibit mean-distortion mode ranking (from largest to smallest) of $R_1^+ > M_5^+ > R_3^+$ whereas the DFT calculated structures show that $R_1^+ > R_3^+ > M_5^+$. We next try to understand this behavior by noting that the R_3^+ and M_5^+ modes act on the same 3*d* oxygen Wyckoff orbit of the high-symmetry cubic phase. As a result, a standard structure refinement would lead to optimization of the sum of these distortions, *i.e.*, their total magnitude in the monoclinic phase. This process, however, does not restrict the contribution of each mode to the total amplitude; different individual mode amplitudes can combine to give the same total magnitude. Routes to circumvent this problem have been recently proposed and rely on using the distortion modes directly in Rietveld refinements.[52] The structure of the nickelates may be a good test for these methods.

These uncertainties in the existing refinements should appear in the variance within the structural data—one expects low standard deviations in the distortion mode amplitudes across the nickelate family based on Vegard's law[53] for isoelectronic substitutions. Here

we find a large variance in the reported distortion mode amplitudes for the experimental structures, whereas a much smaller spread in the amplitudes is found with the DFT structures (Fig. 4). Indeed, for the M_5^+ mode, the variance is larger than the mean value itself, whereas the DFT variance is nearly zero. The tendency for the DFT calculations to describe more uniformly the R cation substitution effects on the distortion mode likely accounts for the DFT reversal in the mean-distortion mode ranking compared to the experiment. Such variance in the experimental data could arise from additional effects beyond the refinement procedures, including temperature effects, secondary phases, or unintentional dopants. Multiple refinements from varying temperatures and synthesis procedures are key to reducing the variance in the structural data. An example chart of the mode amplitudes for $NdNiO_3$ obtained at a single temperature is reported in Table S2, which illustrates the variance typical for one compound with multiple reports in the literature.

From the variance alone, it is unclear if all the structures exhibit equal variance in their mode amplitudes or if a few outliers skew the average. Plotting the raw distortion-mode amplitudes across the nickelate series with respect to the rare earth cation radius R is one way to clarify this effect as we show in Fig. 5a for the a-type R_3^+ Jahn-Teller mode. In the experimental data (round symbols), we find that as the ionic radius increases, the Jahn-Teller mode amplitude counter-intuitively increases until reaching Pr, when the amplitude suddenly decreases. $NdNiO_3$ in particular exhibits a large R_3^+ distortion mode amplitude relative to other rare-earth nickelates. In contrast, the experimental R_1^+ breathing mode amplitude is well-behaved for $NdNiO_3$ and $PrNiO_3$. The anomalous behavior occurs for $DyNiO_3$, whereas for most of the nickelates the R_1^+ breathing mode amplitude decreases with increasing R cation radius (Fig. 5b). The ratio of volumes between neighboring NiO_6 octahedra (Fig. 5c), which serves as a proxy for the R_1^+ breathing mode amplitude, also captures this same behavior. These dichotic trends are difficult to explain if the R cation changes the structure through uniform (homogeneous) steric effects, and indicates

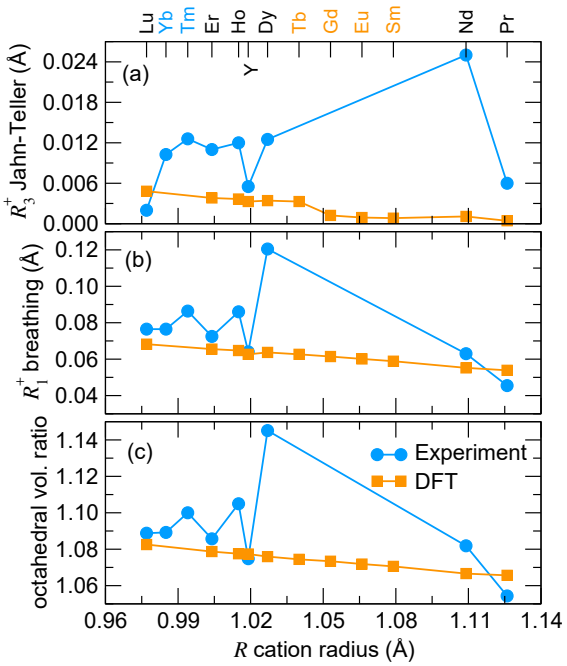

Figure 5: Evolution in the (a) Jahn-Teller mode amplitude, (b) breathing mode amplitude, and (c) ratio of the large-to-small NiO_6 octahedral volumes for the experimental and ground state DFT RNiO$_3$ compounds. R cations in black have both published experimental and theoretically monoclinic structures, whereas those in blue have only experimental structures reported but no published computational structures. R cations in orange correspond to compounds with only calculated structures.

either nontrivial mode-mode interactions or experimental uncertainty. When the ionic radius monotonically increases from Lu to Pr, the distortion mode amplitudes are expected to exhibit a similar monotonic dependence. Indeed, this behavior is captured from the DFT optimized structures, suggesting band-theory is sufficiently accurate to capture the changes in atomic structure with isovalent R cation substitution.

These systematic differences between theoretical and experimental structures indicate the low temperature structural reports in the RNiO$_3$ system merit further scrutiny. This revelation has important consequences. For experimental scientists, the quality of refinements can be improved by comparing local distortions across the compositional family rather than solely minimizing the R-factor (reliability factor) for a single structure. In addition, the presented methodology of distortion-mode-correlation analysis could be extended to explicitly describe local structure as in pair distribution function measurements.[54] For

electronic structure studies, if the property of interest is closely linked to atomic scale structure, such as the band gap or electron effective mass, one cannot assume that property will be in concordance between closely related compositions since their structures might vary discontinuously. Either the experimental structures should be checked for similarity, or from the computational point-of-view, the entire family should be relaxed to be treated on the same footing.

Our last note to emphasize here is that correlations are not enough to show physical relevance. Plotting the values also reveals information about the relative magnitudes of the different distortion modes. In the relaxed structures presented earlier, the mode amplitude of the *a*-type Jahn-Teller R_3^+ distortion mode (Fig. 5a) is an order of magnitude smaller than the breathing R_1^+ distortion mode amplitude (Fig. 5b), likely making its effects essentially negligible to any real ordering transition. Differently in the experimental structures, the *a*-type Jahn-Teller R_3^+ and breathing R_1^+ distortion mode amplitudes are of similar order of magnitude, suggesting that charge and orbital ordering coexist in the $R\mathrm{NiO_3}$ family. This observation, however, is in disagreement with the fact that orbital ordering has never been observed experimentally in $R\mathrm{NiO_3}$.[26,27]

As noted earlier, the two modes appear coexist and compete with each other, with the breathing R_1^+ distortion mode dominant. This competition provides evidence countering the conjecture that the Jahn-Teller R_3^+ mode participates in the metal-insulator and magnetic transitions. Therefore, it is important to view the correlations with some perspective, e.g., given what relative magnitudes of the data features, and the underlying physics in mind. When necessary, one should perform additional calculations or measurements to ensure target quantities change meaningfully over the observed range of composition. We show examples of such calculations in the next section.

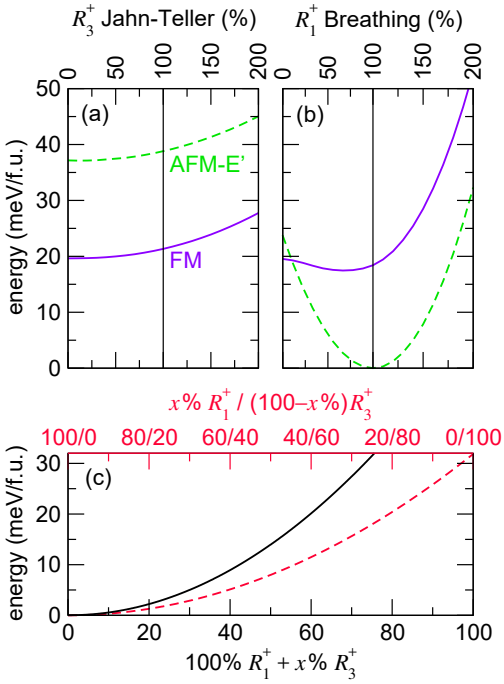

Figure 6: Total energy calculations of different magnetic orders with respect to the NiO_6 octahedral (a) R_3^+ Jahn-Teller and (b) R_1^+ breathing distortion-mode amplitude for $NdNiO_3$. An amplitude of 0 % indicates no distortion and 100 % corresponds to the amplitude of the distortion found in the experimental structure, while larger values indicate increased amplitudes. A crossover in energy, indicative of a possible switch in magnetic order, is only observed with changes in the breathing-mode amplitude. (c) Evolution of the total energy of $NdNiO_3$ with varying percentages of both the R_1^+ and R_3^+ distortion-modes: (solid line, lower abscissa) the R_1^+ breathing mode is constrained to 100 % while the R_3^+ Jahn-Teller mode increases and (broken line, upper abscissa) the R_1^+ mode amplitude decreases (increases) while the R_3^+ mode amplitude increases (decreases). The smaller curvature obtained for the solid line indicates the two distortions are in competition with each other.

Understanding Causation with Electronic-Structure Simulations

We elucidate the causal effects of the R_3^+ Jahn-Teller and R_1^+ breathing modes on the energy scales of the different magnetic orders by performing computational studies in which we perturb the equilibrium structures of the nickelates, focusing on $NdNiO_3$. Firstly, we relaxed the atomic positions of $NdNiO_3$ fixing the cell parameters to the experimental values.[35] As expected from our earlier discussion (Fig. 5), the contribution of the *a*-type Jahn-Teller R_3^+ mode to the overall distortion amplitude is very small. Although finite in the experimental structure, the relaxed structure, nevertheless, shows good agreement

with the experiment. In particular, the breathing R_1^+ mode is well described (see Table S1 of the Supporting Information). Next, we keep fixed the $NdNiO_3$ structure and reduce to zero one distortion mode, R_1^+ or R_3^+, allowing the other one to vary by a fraction of its contribution to the total amplitude given in the experimental structure as shown in Fig. 6a and Fig. 6b, respectively. For each $NdNiO_3$ structure along the aforementioned trajectory, we then compute the energy of the ferromagnetic and AFM-E′ spin orders.

Fig. 6a shows that the Jahn-Teller R_3^+ mode does not change the magnetic order stability; the FM phase is always more stable. In contrast, the breathing R_1^+ mode causes a crossover in energy between the FM and AFM-E′ spin orders (Fig. 6b); the AFM-E′ phase is stabilized at $\sim$25% of the breathing R_1^+ mode amplitude. This change in phase stability with amplitude of the local NiO_6 mode provides strong evidence that the breathing R_1^+ mode is the more physically relevant distortion-mode when discerning the origin for the magnetic phase stability; therefore, its amplitude is likely to be proportional to T_N. Although the *a*CCHMs best describe the equilibrium trends derived from *R*-cation-induced distortions, our computational study can be used to inform experimental efforts aimed at modify the magnetic behavior of nickelates. One could, for example, use non-equilibrium methods, *e.g.*, strain engineering and terahertz excitation, to modify the breathing R_4^+ mode amplitude with the aim of modulating the Néel temperature.

The prior simulation describes the effect of the distortion modes *ceteris paribus* on the magnetic energy scales, but it does not establish the correlation and nature of the interaction between the individual distortion modes in the structure. Therefore, we perform another computational experiment on $NdNiO_3$ whereby we attempt to assess the interaction between the distortion mode pair (R_1^+, R_3^+). We examine the change in total energy for $NdNiO_3$ as (*i*) the R_3^+ mode is increased from 0 to 100% of its experimental value while the R_1^+ mode is held constant, and (*ii*) the R_3^+ is increased while the R_1^+ mode is decreased. The two energy curves for these two scenarios are shown Fig. 6c. A strong competition between the two distortion modes is evident from the difference in curvature $\frac{d^2E}{d\delta^2}$ between

Scenario (*i*) (solid line) and Scenario (*ii*) (broken line). For Scenario 1, where the distortion modes coexist, we find the curvature of the total energy variation with mode amplitude is much higher than in Scenario 2, where the distortion modes compensate one another, *i.e.*, as one increases (*e.g.*, R_1^+) and the other decreases (*e.g.*, R_3^+) and vice versa. These energy variations indicate that the amplitudes of the *a*-type Jahn-Teller R_3^+ and breathing R_1^+ modes should be anti-correlated if the steric effects from the small *R*-cation size are held constant. In other words, the equilibrium state in $NdNiO_3$ prefers to maximize only one of these modes. This explains the observations of others in the literature that the *a*-type Jahn-Teller R_3^+ distortion mode is virtually absent in the theoretical and experimental structures, despite the positive correlation of Jahn-Teller and breathing modes across the nickelate family.[26,27,29] This behavior is also not captured by examining mode–mode correlations obtained from the amplitudes of the published structures alone.

Capturing Interactions from Distortion-Mode–Mode Correlations

Materials design and understanding relies on the capability to assess the key interactions governing properties and performance. Multiple structural degrees of freedom can cooperate or compete to support those interactions. We now show how to discern these distortion-mode–mode dependencies from material structure alone, *e.g.*, without necessarily performing a DFT calculation. In Fig. 7, we plot the *normalized-mode* correlation-coefficient-heat map, hereafter referred to as *n*CCHM, obtained with the DFT structures using the mode amplitudes normalized by the Euclidean norm of the vector defining the complete distortion connecting the $Pm\bar{3}m$ and $P2_1/c$ structures. Here we focus on the DFT structures only owing to the uncertainties discussed earlier regarding the experimental structures, which may obfuscate the analysis.

First, we find that the *n*CCHM gives distortion-mode–property correlations that are opposite to those obtained from the *a*CCHM, *e.g.*, $(R_1^+, T_{MI}) < 0$, whereas the correlation should be positive as in Fig. 2b, to be consistent with the bulk phase diagram. Owing to

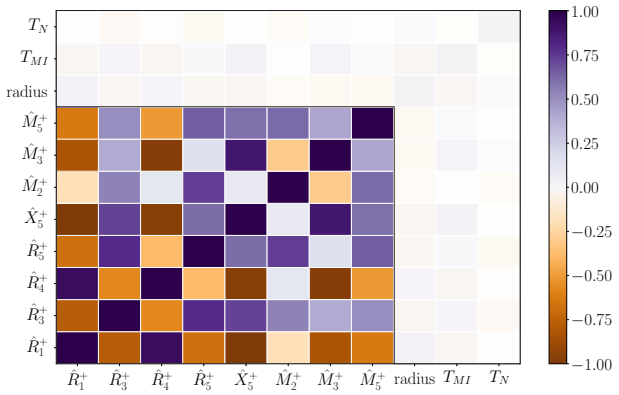

Figure 7: Normalized correlation-coefficient-heat maps (*n*CCHMs) calculated from our DFT relaxed crystal structures. Normalization is indicated by a 'hat' appended to the irrep label and is based on the Euclidean norm of the total mode vector mapping $Pm\bar{3}m \rightarrow P2_1/c$. The white-shade region, screening particular variable pairs, emphasizes the use of *n*CCHMs for understanding distortion-mode–mode correlations and not distortion-mode–property correlations.

these inconsistencies, we find that the distortion-mode–property correlations described by a *n*CCHM should not be used for property predictions and hence are unlikely to be of meaningful purpose. For this reason, we omit these correlations from the heat map appearing in Fig. 7 by screening them with a white-shaded region to emphasize that these correlation pairs should not be used.

On the other hand, we find that the *n*CCHM recovers all of the nuanced mode-mode dependencies in an individual member of the nickelate family upon inspection of the distortion-mode–mode correlations. These correlations as we described below align with the expectations distilled from our DFT calculations and a recent report in the literature.[55] The main differences seen upon comparing the *a*CCHM (Fig. 2b) with the *n*CCHM (Fig. 7) is that the mode–mode correlations are no longer all strongly positive, but rather most mode pairs are anti-correlated. Only a few mode pairs maintain their positive correlation. We understand this complete change as follows: The positive correlations found in the mode amplitude-based *a*CCHMs indicate that when the common perovskite distortion modes are present, such as the NiO_6 octahedral rotation (M_3^+) and tilt (R_4+), then all other symmetry-allowed modes compatible with the orthorhombic *Pnma* and monoclinic $P2_1/c$

symmetries will also be non-zero. The symmetry reductions induced by the small R cation size ensures the existence of these modes, *i.e.*, finite amplitudes of all distortion modes; hence, as the R cation size decreases, these modes all increase (the correlation is positive), which is consistent with the global nickelate phase diagram .

In contrast, the normalized-mode nCCHMs capture the interaction among distortion modes, because the Pearson correlation is now assessing the relative contribution of each mode in the full distortion vector for the nCCHMs to another mode in the compound. Since distortion modes occur to satisfy both local and long-range bond constraints, alleviating bond strain in a bond-valence sense,[56] the normalized modes reveal how much of a given distortion-mode among all possible distortion modes participates in that process. For this reason, the mode-pairs may exhibit positive or negative correlation. For example, particular distortion-modes act on the reference crystal structure in similar fashions. Rotations and tilts of the octhahedra are consistent with this scenario, each reduces the undercoordination of the R cation in similar, but not exactly in the same ways;[57] nonetheless, these two distortion modes can be viewed as competing over the same portion of phase space to satisfy those local bond constraints and realize an energetic gain. Indeed, we find Fig. 7 that the distortion-mode–mode correlation for the pair (R_4^+, M_3^+) is negative indicating that the contribution of the tilt mode increases it is as the expense of the rotation mode, for which its contribution to the total mode-distortion vector would decrease.[55] This anti-correlation is fully consistent with our understanding of the role that octahedral rotations and tilts, which are often described as pseudo-Jahn-Teller distortions, play in stabilizing the distorted perovskite structure.

Anti-correlated mode-mode behavior is also found for the (R_1^+, R_3^+) mode pair in Fig. 7, which is now fully consistent with our domain-science interpretation of the purpose of these two distortions in a rare-earth nickelate. This correlation also corrects the failure of the aCCHM previously discussed. Both the breathing R_1^+ and a-type R_3^+ Jahn-Teller distortion modes remove the orbital degeneracy in different ways to achieve the same purpose; and

for that reason, do in fact compete with one another in an energetic sense towards that goal (Fig. 6). The possible coexistence of these two distortions in the experimental structures may be either an artifact of the structure-refinement or approach (discussed above) or reflect the fact that nickelates are in an intermediate localized electron regime.

Positive correlation, on the other hand, persists for the (R_1^+, R_4^+) mode pair (Fig. 7), indicating that as the contribution of NiO_6 octhahedral tilts in the structure increase so does the contribution of the NiO_6 breathing R_1^+ mode. This can be understood by noting that finite octahedral rotations affect the electronic structure by reducing the frontier-orbital bandwidth, which is an established route to achieve metal-insulator transitions.[58] As the bandwidth decreases (through changes in the structure), the electronic mechanism (and its own associated structural manifestation) is similarly activated. Interestingly, owing to the $(R_4^+, M_3^+) < 0$ correlation, we also find that $(R_1^+, M_3^+) < 0$, which supports the recent view that the electronic transition is triggered by anharmonic tilt-rotation-breathing mode distortions in the nickelates.[55] Remarkably, this interaction gleaned from the data-driven structural analysis is almost achieved computationally for free without the need of sophisticated and compute-intensive electronic structure calculations.

Applicability to database screening

As we have demonstrated, mode crystallography is a powerful tool for formulating structure–property relationships, but its use in high-throughput workflows is limited by a lack of available, easy-to-use software packages. There are other alternative methods, nonetheless, developed to assess the consistency of local structure–property responses computationally, such as those contained in the `Pymatgen` software package.[59] A possible workflow for analyzing the role of local structure on the properties of complex crystal structures, such as in the nickelate family described above, with some of these tools illustrated is in Fig. 8. In addition, all steps given here can be explored in the Jupyter Notebooks available in the SI.

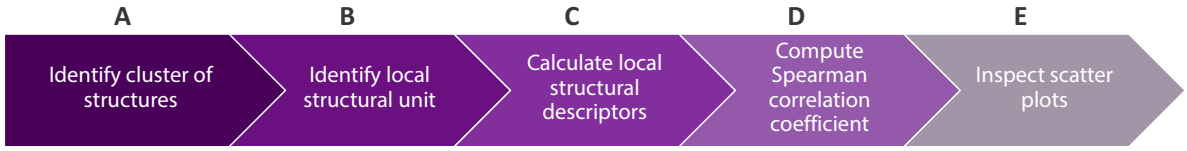

Figure 8: Schematic workflow by Step (given in bold) to assess the role of local structure in material properties.

In Step A, one first ascertains clusters of similar structures. This can be accomplished by expert-created whitelists of known groups (*e.g.*, rare-earth nickelates), by comparing data-mined measures of substructural similarity[60] or by using the StructureMatcher class within `Pymatgen`,[59] which checks if structures match within length, angle, and site tolerances. Next in Step B, the local structural units of interest (*e.g.*, metal-oxygen octahedra) are identified through either expert knowledge, Voronoi tesselation,[61] or other nearest-neighbor searches based on distance. Once the local unit is identified, Step C involves computing local structural descriptors such as polyhedral volume, bond lengths, and bond angles. These quantities can be combined into appropriate statistical forms to measure the amplitudes of distortion modes of interest, *e.g.*, for measuring polyhedral breathing distortions. Here, the ratio of the maximum polyhedral volume to the minimum polyhedral volume correlates nearly exactly with the breathing R_1^+ mode amplitude (Fig. 5). When the amount of information is too large to screen manually, the Spearman rank correlation coefficient should be computed between rare earth ionic radius and the local structural features (Step D). The Spearman correlation coefficient measures how well the relationship between two variables can be described by a monotonic function. If the descriptor always increases (decreases) with an increase in ionic radius, the coefficient will be $+1$ (-1). If the descriptor is nonlinear, the Spearman correlation coefficient will be close to 0. Descriptors with a correlation-coefficient magnitude smaller than 0.8 should be examined for visual inspection by experts (Step E).

We use the antipolar X_5^+ distortion mode in the rare-earth nickelate series to demonstrate our proposed workflow (Fig. 8). This mode shows up in a lighter shade of blue

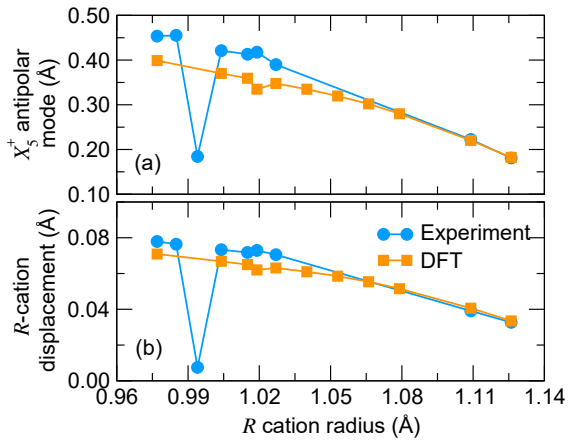

Figure 9: (a) Antipolar distortion-mode amplitudes for the RNiO$_3$ family using experimental and DFT-relaxed structures. (b) The displacement of the rare-earth cation captures the same trend of the distortion X_5^+ mode amplitude.

than its neighbors in Fig. 2a, indicating unexpected behavior. In this case, the structural cluster (Step A), rare-earth nickelates, is identified through prior knowledge, but the `group_structure` method would also work here. The local structural unit is identified in Step B through a nearest-neighbors method as the NiO$_6$ octahedra, but prior knowledge produces the same conclusion. Since the antipolar X_5^+ distortion mode involves the displacement of R cations (Fig. 1), their displacements in the crystallographic b direction is used as the local structural descriptor (Step C). The Spearman correlation coefficient of the R cation displacement with ionic radius is -0.63 for the experimental structures and -0.99 for the theoretical structures (Step D). Since the correlation-coefficient magnitude for the experimental structures falls below 0.8, we generate its corresponding the scatter plot in Fig. 9 (Step E). The values for the theoretical structures are given in orange. For comparison, we also show the X_5^+ mode amplitude in Fig. 9. The R-site displacement serves as an excellent descriptor, capturing the smooth downward trend aside from the deviation seen in TmNiO$_3$. The similar magnitudes of the orange and blue curves also indicate the experimental structure refinements and first principles structural relaxations are in good agreement for the size of this particular antipolar distortion.

Conclusions

With the propagation of machine-learning methods for use in materials chemistry, we have re-examined the applicability of correlation maps constructed from distortion-mode–property pairs within the rare earth nickelate family. We show that both the number and quality of the data, *i.e.*, the sparsity of and uncertainty in the crystal structures, and applying a naïve interpretation of the heat maps can lead to incorrect inferences on the role of local structure in governing material properties. The nuances associated with constructing distortion-mode–property relationships are demonstrated by clarifying that the distortion modes can be used in correlation-coefficient heat maps (CCHMs) in two distinct ways: first, by using the amplitudes of the distortion modes, which we referred to as *a*CCHMs, and second, by using normalized-distortion modes, *n*CCHMs, which represent the relative contribution of each distortion present among all modes present.

We found that the *a*CCHMs reproduce the global dependencies observed in the rare-earth nickelate phase diagram, captured in a numerical manner, making these maps suitable for understanding distortion-mode–property relationships and their evolution with uniform perturbations, such as chemical pressure (R cation size) and hydrostatic pressure. The *a*CCHMs are of limited use in identifying subtler, but physically relevant, mode-mode interactions, but these nuances can be deduced from the *n*CCHMs. Furthermore, the *n*CCHMs can be used to understand local mode-mode dependencies within a single composition, as we show for $NdNiO_3$ and can guide experiments using non-isotropic perturbations, e.g., epitaxial strain in thin films and nonlinear phononic control with ultra-fast light pulses. At this time, the absence of direct reciprocity and applicablity between the CCHMs merits further attention and the analyses we have performed should be pursued in other families of transition metal compounds exhibiting multiple electronic and structure degrees of freedom. To that end, we recommend that the data-represented in CCHMs and the manner in which it is processed be clearly described, thereby allowing for proper materials chemistry inferences. These correlation-coefficient-heat maps should

also be views as a useful starting point for further computation- and experiment-driven investigations of structure-property relationships aimed at understanding the microscopic interactions governing the dependencies.

In summary, we demonstrated how computational experiments can improve the usefulness of data-mining techniques in the materials domain and its identification of potential anomalous crystal structures. Because the observed correlations between structure and properties are only as powerful as the data they are built upon, we specifically recommend that additional experimental structure refinements be performed on some of the low-temperature $P2_1/c$ monoclinic $R\mathrm{NiO_3}$. Based on the aforementioned analyses, we then proposed a computational method for identifying structural anomalies that is not explicitly dependent upon representation theory. Last, we hope the demonstrated utility of mode crystallography in statistical descriptions of local structure leads to further developments in the materials chemistry field and its application to interrogating large structural databases.

Supporting Information

The Supporting Information is available free of charge on the ACS Publications website at DOI: XXXXXXX.

Distortion-mode and ordering temperature scatter plots for the experimental and DFT calculated structures, experimental nCCHM, distortion-mode details for $\mathrm{NdNiO_3}$, Jupyter notebooks, and the perovskite nickelate database.

Acknowledgement

N.W. and J.M.R. were supported by the National Science Foundation (NSF) under award no. DMR-1729303. D.P. was supported by the Army Research Office (ARO) under award

no. W911NF-15-1-0017. Calculations were performed using the QUEST HPC facility at Northwestern, the HPC facility at the Extreme Science and Engineering Discovery Environment (XSEDE) of the NSF (ACI-1548562), and the DOD-HPCMP. The authors thank P. Balachandran for useful discussions.

Conflict of Interest

The authors declare they have no conflicting interests.

References

(1) Hill, J.; Mannodi-Kanakkithodi, A.; Ramprasad, R.; Meredig, B. In *Computational Materials System Design*; Shin, D., Saal, J., Eds.; Springer International Publishing, 2018; Chapter 9, pp 193–225.

(2) Ward, L.; Wolverton, C. Atomistic Calculations and Materials Informatics: A Review. *Curr. Opin. Solid State Mater. Sci.* **2017**, *21*, 167–176.

(3) Ramprasad, R.; Batra, R.; Pilania, G.; Mannodi-Kanakkithodi, A.; Kim, C. Machine Learning in Materials Informatics: Recent Applications and Prospects. *npj Comput. Mater.* **2017**, *3*, 54.

(4) Hellenbrandt, M. The Inorganic Crystal Structure Database (ICSD)—Present and Future. *Crystallogr. Rev.* **2004**, *10*, 17–22.

(5) Gražulis, S.; Chateigner, D.; Downs, R. T.; Yokochi, A. F. T.; Quirós, M.; Lutterotti, L.; Manakova, E.; Butkus, J.; Moeck, P.; Le Bail, A.; IUCr, Crystallography Open Database – an Open-access Collection of Crystal Structures. *J. Appl. Crystallogr.* **2009**, *42*, 726–729.

(6) Gražulis, S.; Daškevič, A.; Merkys, A.; Chateigner, D.; Lutterotti, L.; Quirós, M.; Serebryanaya, N. R.; Moeck, P.; Downs, R. T.; Le Bail, A. Crystallography Open

Database (COD): an Open-access Collection of Crystal Structures and Platform for World-wide Collaboration. *Nucleic Acids Res.* **2012**, *40*, D420–D427.

(7) He, L.; Liu, F.; Hautier, G.; Oliveira, M. J. T.; Marques, M. A. L.; Vila, F. D.; Rehr, J. J.; Rignanese, G.-M.; Zhou, A. Accuracy of Generalized Gradient Approximation Functionals for Density-functional Perturbation Theory Calculations. *Phys. Rev. B* **2014**, *89*, 064305.

(8) Haas, P.; Tran, F.; Blaha, P. Calculation of the Lattice Constant of Solids with Semilocal Functionals. *Phys. Rev. B* **2008**, *79*, 85104.

(9) Cozzan, C.; Laurita, G.; Gaultois, M. W.; Cohen, M.; Mikhailovsky, A. A.; Balasubramanian, M.; Seshadri, R. Understanding the Links Between Composition, Polyhedral Distortion, and Luminescence Properties in Green-emitting β-$Si_{6-z}Al_zO_zN_{8-z}$:Eu^{2+} Phosphors. *J. Mater. Chem. C* **2017**, *5*, 10039–10046.

(10) Young, J. Design of Noncentrosymmetric Perovskites from Centric and Acentric Basic Building Units. *J. Mater. Chem. C* **2016**, *4*, 4016-4027.

(11) Isayev, O.; Fourches, D.; Muratov, E. N.; Oses, C.; Rasch, K.; Tropscha, A.; Curtarolo, S. Materials Cartography: Representing and Mining Material Space Using Structural and Electronic Fingerprints. *Chem. Mater.* **2015**, *27*, 735–743.

(12) Huo, H.; Rupp, M. Unified Representation for Machine Learning of Molecules and Crystals. *arXiv preprint* **2017**, 1704.06439.

(13) Ward, L.; Liu, R.; Krishna, A.; Hegde, V. I.; Agrawal, A.; Choudhary, A.; Wolverton, C. Including Crystal Structure Attributes in Machine Learning Models of Formation Energies via Voronoi Tessellations. *Phys. Rev. B* **2017**, *96*, 024104.

(14) Xie, T.; Grossman, J. C. Crystal Graph Convolutional Neural Networks for an Accurate and Interpretable Prediction of Material Properties. *Phys. Rev. Lett.* **2018**, *120*, 145301.

(15) Howard, C. J.; Stokes, H. T. Group-Theoretical Analysis of Octahedral Tilting in Perovskites. *Acta Crystallogr. B* **1998**, *54*, 782–789.

(16) Campbell, B. J.; Stokes, H. T.; Tanner, D. E.; Hatch, D. M. ISODISPLACE: A Web-based Tool for Exploring Structural Distortions. *J. Appl. Crystallogr.* **2006**, *39*, 607–614.

(17) Perez-Mato, J. M.; Orobengoa, D.; Aroyo, M. I. Mode Crystallography of Distorted Structures. *Acta Crystallogr. A* **2010**, *66*, 558–590.

(18) Attfield, J. P. Charge Ordering in Transition Metal Oxides. *Solid State Sci.* **2006**, *8*, 861–867.

(19) Rodríguez-Martínez, L. M.; Attfield, J. P. Disorder-induced Orbital Ordering in $La_{0.7}Mn_{0.3}MnO_3$ Perovskites. *Phys. Rev. B* **2000**, *63*, 024424.

(20) Senn, M. S.; Wright, J. P.; Attfield, J. P. Charge Order and Three-site Distortions in the Verwey Structure of Magnetite. *Nature* **2012**, *481*, 173–176.

(21) Rodríguez-Martínez, L. M.; Rodriguez-Martinez, L. M.; Attfield, J. P. Cation Disorder and the Metal-insulator Transition Temperature in Manganese Oxide Perovskites. *Phys. Rev. B* **1998**, *58*, 2426.

(22) Balachandran, P. V.; Benedek, N. A.; Rondinelli, J. M. In *Information Science for Materials Discovery and Design*; Lookman, T., Alexander, F. J., Rajan, K., Eds.; Springer Series in Materials Science; Springer International Publishing, 2016; Vol. 225; pp 213–222.

(23) Medarde, M. L. Structural, Magnetic and Electronic Properties of RNiO3 Perovskites (R = Rare Earth). *J. Phys. Condens. Matter* **1997**, *9*, 1679–1707.

(24) Rościszewski, K.; Oleś, A. M. Jahn–Teller Distortions and the Magnetic Order in the Perovskite Manganites. *J. Phys. Condens. Matter* **2010**, *22*, 425601.

(25) Mazin, I. I.; Khomskii, D. I.; Lengsdorf, R.; Alonso, J. A.; Marshall, W. G.; Ibberson, R. M.; Podlesnyak, A.; Martínez-Lope, M. J.; Abd-Elmeguid, M. M. Charge Ordering as Alternative to Jahn-Teller Distortion. *Phys. Rev. Lett.* **2007**, *98*, 176406.

(26) Scagnoli, V.; Staub, U.; Mulders, A. M.; Janousch, M.; Meijer, G. I.; Hammerl, G.; Tonnerre, J. M.; Stojic, N. Role of Magnetic and Orbital Ordering at the Metal-insulator Transition in $NdNiO_3$. *Phys. Rev. B* **2006**, *73*, 100409.

(27) Rodríguez-Carvajal, J.; Rosenkranz, S.; Medarde, M.; Lacorre, P.; Fernandez-Díaz, M. T.; Fauth, F.; Trounov, V. Neutron-diffraction Study of the Magnetic and Orbital Ordering in ^{154} $SmNiO_3$ and $^{153}EuNiO_3$. *Phys. Rev. B* **1998**, *57*, 456–464.

(28) Balachandran, P. V.; Rondinelli, J. M. Interplay of Octahedral Rotations and Breathing Distortions in Charge-ordering Perovskite Oxides. *Phys. Rev. B* **2013**, *88*, 054101.

(29) Varignon, J.; Grisolia, M. N.; Íñiguez, J.; Barthélémy, A.; Bibes, M. Complete Phase Piagram of Rare-earth Nickelates from First-principles. *npj Quant. Mater.* **2017**, *2*, 21.

(30) Wagner, N.; Rondinelli, J. M. Theory-Guided Machine Learning in Materials Science. *Front. Mater.* **2016**, *3*, 28.

(31) Kresse, G.; Furthmüller, J. Efficiency of Ab-initio Total Energy Calculations for Metals and Semiconductors Using a Plane-wave Basis Set. *Comput. Mater. Sci.* **1996**, *6*, 15–50.

(32) Perdew, J. P.; Ruzsinszky, A.; Csonka, G. I.; Vydrov, O. A.; Scuseria, G. E.; Constantin, L. A.; Zhou, X.; Burke, K. Restoring the Density-Gradient Expansion for Exchange in Solids and Surfaces. *Phys. Rev. Lett.* **2008**, *100*, 136406.

(33) Dudarev, S. L.; Botton, G. A.; Savrasov, S. Y.; Humphreys, C. J.; Sutton, A. P. Electron-energy-loss Spectra and the Structural Stability of Nickel Oxide: An LSDA+U Study. *Phys. Rev. B* **1998**, *57*, 1505–1509.

(34) Hampel, A.; Ederer, C. Interplay Between Breathing Mode Distortion and Magnetic Order in Rare-earth Nickelates $RNiO_3$ within DFT+U. *Phys. Rev. B* **2017**, *96*, 165130.

(35) Garcia-Muñoz, J. L.; Aranda, M. A. G.; Alonso, J. A.; Martinez-Lope, M. J. Structure and Charge Order in the Antiferromagnetic Band-insulating Phase of $NdNiO_3$. *Phys. Rev. B* **2009**, *79*, 134432.

(36) Mizokawa, T.; Khomskii, D. I.; Sawatzky, G. A. Spin and Charge Ordering in Self-doped Mott Insulators. *Phys. Rev. B* **2000**, *61*, 11263–11266.

(37) Orobengoa, D.; Capillas, C.; Aroyo, M. I.; Perez-Mato, J. M. AMPLIMODES: Symmetry-mode Analysis on the Bilbao Crystallographic Server. *J. Appl. Crystallogr.* **2009**, *42*, 820–833.

(38) Aroyo, M. I.; Kirov, A.; Capillas, C.; Perez-Mato, J. M.; Wondratschek, H. Bilbao Crystallographic Server. II. Representations of Crystallographic Point Groups and Space Groups. *Acta Cryst. A* **2006**, *A62*, 115–128.

(39) Alonso, J. A.; Martínez-Lope, M. J.; Casais, M. T.; García-Muñoz, J. L.; Fernández-Díaz, M. T. Room-temperature Monoclinic Distortion due to Charge Disproportionation in $RNiO_3$ Perovskites with Small Rare-earth Cations (R = Ho , Y, Er, Tm, Yb, and Lu): A Neutron Diffraction Study. *Phys. Rev. B* **2000**, *61*, 1756–1763.

(40) Medarde, M.; Fernández-Díaz, M. T.; Lacorre, P. Long-range Charge Order in the Low-temperature Insulating Phase of $PrNiO_3$. *Phys. Rev. B* **2008**, *78*, 212101.

(41) Muñoz, A.; Alonso, J. A.; Martínez-Lope, M. J.; Fernández-Díaz, M. T. On the Magnetic Structure of $DyNiO_3$. **2009**, *182*, 1982–1989.

(42) Catalan, G. Progress in Perovskite Nickelate Research. *Phase Transitions* **2008**, *81*, 729–749.

(43) Shannon, R. D. Revised Effective Ionic Radii and Systematic Studies of Interatomic Distances in Halides and Chalcogenides. *Acta Crystallogr. A* **1976**, *32*, 751–767.

(44) Grimes, R. Database of Ionic Radii. `http://abulafia.mt.ic.ac.uk/shannon/`urldate = 2018-03-15.

(45) Jones, E.; Oliphant, T.; Peterson, P. SciPy: Open Source Scientific Tools for Python. 2001; `http://www.scipy.org`, urldate = 2018-03-16.

(46) Oliphant, T. E. *Guide to NumPy*; Trelgol, 2006.

(47) Hunter, J. D. Matplotlib: A 2D graphics Environment. *Comput. Sci. Eng.* **2007**, *9*, 90–95.

(48) Plotly, Collaborative Data Science. 2015; `https://plot.ly`, urldate = 2018-03-15.

(49) Momma, K.; Izumi, F.; IUCr, VESTA 3 for Three-dimensional Visualization of Crystal, Volumetric and Morphology Data. *J. Appl. Crystallogr.* **2011**, *44*, 1272–1276.

(50) Alonso, J. A.; Martínez-Lope, M. J.; Presniakov, I. A.; Sobolev, A. V.; Rusakov, V. S.; Gapochka, A. M.; Demazeau, G.; Fernández-Díaz, M. T. Charge Disproportionation in $RNiO_3$ (R = Tm, Yb) Perovskites Observed in situ by Neutron Diffraction and ^{57}Fe Probe Mössbauer Spectroscopy. *Phys. Rev. B* **2013**, *87*, 184111.

(51) Rusakov, V. S.; Presniakov, I. A.; Gapochka, A. M.; Sobolev, A. V.; Tolmachev, T. D.; Lukyanova, E. N. Hyperfine Interactions of ^{57}Fe Impurity Nuclei in $TmNiO_3$ and $YbNiO_3$ Nickelates in the Range of Magnetic and Structure Phase Transitions. Proceedings of the 12th International Conference "Mössbauer Spectroscopy and its Applications". 2013; pp 672–677.

(52) Kerman, S.; Campbell, B. J.; Satyavarapu, K. K.; Stokes, H. T.; Perselli, F.; Evans, J. S. O. The Superstructure Determination of Displacive Distortions *via* Symmetry-mode Analysis. *Acta Crystallographica Section A* **2012**, *68*, 222–234.

(53) Denton, A. R.; Ashcroft, N. W. Vegard's law. *Phys. Rev. A* **1991**, *43*, 3161–3164.

(54) Fry-Petit, A. M; Rebola, A. F; Mourigal, M.; Valentine, M.; Drichko, N.; Sheckelton, J. P.; Fennie, C. J.; McQueen, T. M. Direct Assignment of Molecular Vibrations via Normal Mode Analysis of the Neutron Dynamic Pair Distribution Function Technique. *J. Chem. Phys.* **2015**, *143*, 124201.

(55) Mercy, A.; Bieder, J.; Íñiguez, J.; Ghosez, P. Structurally Triggered Metal-insulator Transition in Rare-earth Nickelates. *Nat. Commun.* **2017**, *8*, 1677.

(56) Lufaso, M. W.; Woodward, P. M. Jahn–Teller Distortions, Cation Ordering and Octahedral Tilting in Perovskites. *Acta Cryst. B* **2004**, *60*, 10–20.

(57) Cammarata, A.; Rondinelli, J. M. Covalent Dependence of Octahedral Rotations in Orthorhombic Perovskite Oxides. *J. Chem. Phys.* **2014**, *141*, 114704.

(58) Imada, M.; Fujimori, A.; Tokura, Y. Metal-insulator Transitions. *Reviews of Modern Physics* **1998**, *70*, 1039–1263.

(59) Ong, S. P.; Richards, W. D.; Jain, A.; Hautier, G.; Kocher, M.; Cholia, S.; Gunter, D.; Chevrier, V. L.; Persson, K. A.; Ceder, G. Python Materials Genomics (pymatgen): A Robust, Open-source Python Library for Materials Analysis. *Comput. Mater. Sci.* **2013**, *68*, 314–319.

(60) Yang, L.; Dacek, S.; Ceder, G. Proposed Definition of Crystal Substructure and Substructural Similarity. *Phys. Rev. B* **2014**, *90*, 54102.

(61) Waroquiers, D.; Gonze, X.; Rignanese, G.-M.; Welker-Nieuwoudt, C.; Rosowski, F.; Göbel, M.; Schenk, S.; Degelmann, P.; Andre, R.; Glaum, R.; Hautier, G. Statistical Analysis of Coordination Environments in Oxides. *Chem. Mater.* **2017**, *29*, 8346–8360.

Table of Contents Entry